

Biomimetic artificial Si compound eye surface structures with broadband and wide-angle antireflection properties for Si-based optoelectronic applications†

Cite this: *Nanoscale*, 2013, 5, 10455

Jung Woo Leem,^a Young Min Song^b and Jae Su Yu^{*a}

We report the biomimetic artificial silicon (Si) compound eye structures for broadband and wide-angle antireflection by integrating nanostructures (NSs) into periodically patterned microstructures (p-MSs) via thermal dewetting of gold and subsequent dry etching. The truncated cone microstructures with a two-dimensional hexagonal symmetry pattern were fabricated by photolithography and dry etching processes. The desirable shape and density of the nanostructures were obtained by controlled dewetting. The incorporation of p-MSs into the NS/Si surface further reduced the surface total reflectance over a wide wavelength range of 300–1030 nm at near normal incidence, indicating the average reflectance (R_{avg}) and solar weighted reflectance (R_{SWR}) values of $\sim 2.5\%$ and 2% , respectively, compared to the only NSs on the flat Si surface (*i.e.*, $R_{\text{avg}} \sim 4.9\%$ and $R_{\text{SWR}} \sim 4.5\%$). Additionally, the resulting structure improved the angle-dependent antireflection property due to its relatively omnidirectional shape, which exhibited the $R_{\text{avg}} < 4.3\%$ and $R_{\text{SWR}} < 3.7\%$ in the wavelength region of 300–1100 nm even at a high incident light angle of 70° in the specular reflectance.

Received 30th May 2013

Accepted 19th August 2013

DOI: 10.1039/c3nr02806b

www.rsc.org/nanoscale

Introduction

Biomimetic compound eyes have attracted much interest in the various fields of optics, optoelectronics, and biology because of their multi-functions including fast image processing capability, self-cleaning ability of lotus leaves, antifogging, large field of view, and broadband antireflection.^{1–4} For the compound eyes of insects, the cornea surface structure is usually composed of thousands of two-dimensional (2D) hexagonal microstructures with nipple arrayed nanostructures. In the view of optical properties, the omnidirectionally aligned microstructures allow for suppressing the surface reflection for obliquely incident light as well as focusing the incident light towards the photoreceptor cells. On the other hand, the nanostructures with a smaller period than the incident light wavelength can effectively reduce the Fresnel surface reflection in the wide ranges of wavelengths and incident angles because they act as an effective homogeneous medium with a linearly and continuously graded refractive index profile between air and the surface.⁵ Thus, the compound eye structures are expected to further reduce the surface reflection losses for any

incident angle including normal incidence. Recently, the thermal dewetting of thin metal films, which is one of the useful, simple, and low-cost nanopatterning processes compared to the electron beam or nanoimprint lithography, is widely used to form nanoscale metal particles over a large area as an etch mask for pattern transfer with dry etching in the fabrication of nanostructures.^{6–9}

Meanwhile, silicon (Si) is one of the important elemental materials used in various optoelectronic devices such as solar cells, photodetectors, and image sensors.^{10,11} However, Si has a high reflectivity, related to its refractive index ($n_{\text{Si}} > 3.4$) at visible and IR wavelengths, which can degrade the device performance owing to the optical losses caused by Fresnel surface reflection. Thus, it is necessary to employ efficient antireflection coatings on the surface of Si-based optoelectronic devices. Therefore, it is very meaningful to investigate the surface reflection of the compound eye structure consisting of the nanonipple arrays on the microstructured Si surface. In this work, we investigated the structural and optical properties of the artificial compound eyes consisting of the nanostructures (NSs) on the top of the periodic microstructures (p-MSs) on Si (*i.e.*, p-MS/Si) substrates, fabricated using the photolithographic photoresist (PR) micropatterns and thermally dewetted gold (Au) nanopatterns for inductively coupled plasma (ICP) dry etching. The angle-dependent specular reflectance characteristics were also studied. For the fabricated samples, the optical reflection properties were theoretically investigated using the rigorous coupled-wave analysis (RCWA) method.

^aDepartment of Electronics and Radio Engineering, Kyung Hee University, 1 Seocheon-dong, Giheung-gu, Yongin-si, Gyeonggi-do 446-701, Republic of Korea. E-mail: jsyu@khu.ac.kr; Fax: +82-31-206-2820; +82-31-201-3820

^bDepartment of Electronic Engineering, Pusan National University 2, Busandaehak-ro 62 beon-gil, Geumjeong-gu, Busan 609-735, Republic of Korea

† Electronic supplementary information (ESI) available: See DOI: 10.1039/c3nr02806b

Experimental and simulation modelling details

The schematic diagram of process steps for fabricating the compound eye architectures consisting of NSs on p-MS/Si substrates is illustrated in Fig. 1. The 30°- and 80°-tilted oblique-view scanning electron microscopy (SEM) images of the thermally reflowed lens-like PRs with 2D hexagonal periodic micropatterns and the etched p-MSs on the Si substrate are also shown in Fig. 1. To fabricate Si compound eye structures, 4 inch single-side polished (100) Si wafers were used. The Si wafer was cut into several pieces with a size of $2 \times 2 \text{ cm}^2$ and then cleaned in acetone and methanol, rinsed in de-ionized water, and subsequently dried in flowing nitrogen (N_2) gas. For the p-MSs, the 2D hexagonal periodic PRs were formed on Si substrates by photolithography, and then they were thermally reflowed to fabricate the closely packed lens-like patterns on a hot plate at a temperature of 200 °C for 90 s. Subsequently, the samples were etched by ICP etching in sulphur hexafluoride (SF_6) plasma. The dry etching was performed with 100 W RF power at 10 mTorr for 10 min in an SF_6 gas flow rate of 10 sccm, creating the truncated cone MSs with the average height and period of ~ 1 and $5 \mu\text{m}$ on Si substrates. As shown in the SEM image of Fig. 1, it can be observed that the periodic lens-like PR patterns and truncated cone MSs were well fabricated on Si substrates. The remaining PR residues were removed by an oxygen plasma process. For the NSs, the Au thin films with different thicknesses of 5, 10, and 15 nm were deposited on the fabricated p-MS/Si substrates by thermal evaporation. To obtain the dot-like nanoparticles as an etch mask pattern, the samples were thermally treated by rapid thermal annealing at a temperature of 600 °C for 60, 120, and 180 s for Au film thicknesses of 5, 10, and 15 nm, respectively, in a N_2 environment. During the thermal dewetting process, the Au thin films are agglomerated into the nanoscale particles to minimize the surface free energy, which results from the increased surface energy of Au by the heating, like the mechanism of Ostwald ripening.^{12,13} To maintain the similar height and shape of p-MSs on Si substrates, the dry etching process

was carried out at the same time for the samples with different Au film thicknesses. The etching conditions of 25 W RF power and additional 100 W ICP power were used at 10 mTorr for 10 min at a tetrachloride (SiCl_4) gas flow rate of 5 sccm. After the etching, the remaining Au residues were removed using an Au etchant. The surface morphology and etched profiles of the fabricated samples were observed using a SEM (LEO SUPRA 55, Carl Zeiss). The total reflectance was measured by using a UV-vis-NIR spectrophotometer (Cary 500, Varian) with an integrating sphere at a near-normal incident angle of $\sim 8^\circ$. The angle-dependent reflectance was investigated using a Cary variable angle specular reflectance accessory at incident angles of 20–70° for un-polarized light.

The theoretical analysis of the optical properties of the fabricated Si compound eye structures consisting of the NSs on p-MSs was carried out using the RCWA method *via* commercial software (*DiffractionMOD* 3.1, Rsoft Design Group).^{14,15} To design the theoretical models, both the MSs and NSs were roughly represented by a periodic geometry with a 2D hexagonal pattern in the Cartesian coordinate system by a scalar-valued function of three variables, $f(x, y, z)$, for simplicity. In calculations, it was assumed that the un-polarized incident light enters the structure from air at normal incidence (see Fig. S1 in the ESI†).

Results and discussion

Fig. 2 shows the SEM images of (a) the thermally dewetted Au nanopatterns (top view) and (b) the fabricated NSs (30°-tilted oblique view) on p-MS/Si substrates for different Au film thicknesses of 5, 10, and 15 nm, respectively. It can be observed that the dot-like Au nanoparticles were well formed on the p-MS/Si substrates for all the Au films, as shown in Fig. 2(a). Using a public domain image processing program (ImageJ 1.42q, NIH), the average densities of the thermally dewetted Au nanoparticles were analyzed, exhibiting 56.8, 50.3, and 34.5% for Au film thickness of 5, 10, and 15 nm, respectively. The average diameter and period of Au nanoparticles were estimated to be 40 ± 5 , 160 ± 20 , and $230 \pm 45 \text{ nm}$ and 50, 210, and 360 nm for 5, 10, and 15 nm, respectively. The density, size, and period of thermally dewetted Au nanopatterns as the etch mask can be roughly controlled by adjusting the Au film thickness.⁶

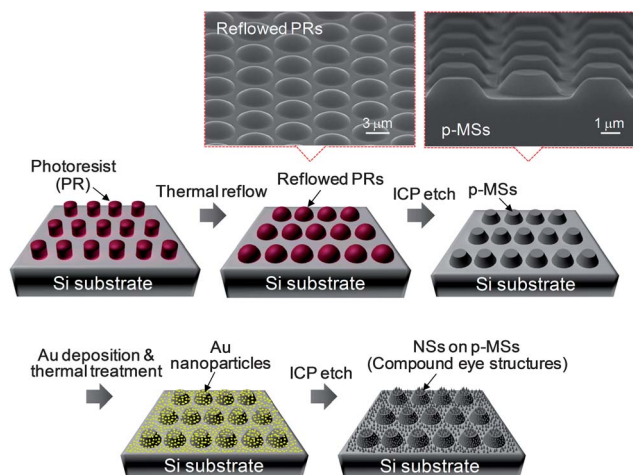


Fig. 1 Schematic diagram of process steps for fabricating the compound eye architectures consisting of NSs on p-MS/Si substrates. The 30°- and 80°-tilted oblique-view SEM images of the thermally reflowed lens-like PRs with 2D hexagonal periodic micropatterns and the etched p-MSs on the Si substrate are also shown.

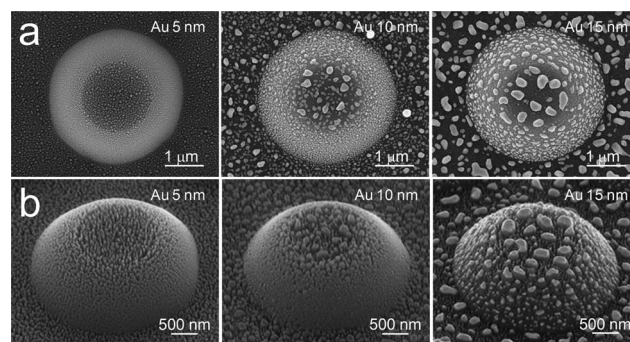


Fig. 2 SEM images of (a) the thermally dewetted Au nanopatterns (top view) and (b) the fabricated NSs (30°-tilted oblique view) on p-MS/Si substrates for different Au film thicknesses of 5, 10, and 15 nm, respectively.

The Au nanopatterns were transferred directly into the underlying surface of the p-MS/Si substrates by dry etching, which produces the compound eye structures consisting of the NSs on p-MS/Si substrates, as can be seen in Fig. 2(b). All the NSs roughly showed a truncated cone shape with an average height of ~ 200 nm. This low height of NSs is caused by the limitations due to the relatively small size and low thickness of the thermally dewetted Au nanopatterns as the etch mask for the thinnest Au film thickness of 5 nm in this experiment to keep their similar height as well as the shape and height of MSs for all the samples. Meanwhile, at the side walls of the p-MSs, the NSs with relatively very low heights were formed compared to the flat region. This is the reason why the smaller Au nanoparticles were formed at the side walls compared to those at the flat surface of the p-MS/Si substrates and so they are removed more quickly.

Fig. 3 shows the (a) measured total reflectance spectra of the fabricated NSs on p-MS/Si substrates for different Au film thicknesses of 5, 10, and 15 nm, (b) contour plot of variations of calculated total reflectance as functions of the period of NSs and wavelength for the NSs on the flat Si substrate, and (c) electric field (E-field) intensity distributions of (i) the flat Si substrate, (ii) the p-MS/Si substrate, and (iii) the NSs on the flat Si substrate. The insets of Fig. 3(a) show the measured (solid lines) and calculated (dashed lines) total reflectance spectra (left) of the flat Si substrate and the p-MS/Si substrate and the 30° -tilted oblique- and side-view SEM images (right) of the fabricated NSs on the flat Si substrate for the Au film thickness of 10 nm. For comparison, the measured total reflectance spectrum (red dashed line) of the NSs on the flat Si substrate is also shown in Fig. 3(a). In the wavelength range above $\lambda \sim 1030$ nm, a rapid increase in the reflectance spectra was observed for all the samples including the Si substrate due to the backscattering of light by the reflection from the back surface of the Si substrate.¹⁶ For the truncated cone p-MSs with a height of $1 \mu\text{m}$, it slightly reduced the reflectance compared to the flat Si substrate, indicating the average reflectance (R_{avg}) of $\sim 34.7\%$ in the wavelength range of 300–1030 nm (i.e., $R_{\text{avg}} \sim 38.1\%$ for the flat Si substrate). The 3D simulation model of the p-MSs used in this calculation is illustrated in Fig. S1(a) of the ESI.† As can be seen in the left inset of Fig. 3(a), the calculated total reflectance spectra are in good agreement with the experimentally measured results. In contrast, all the NSs on p-MS/Si substrates effectively suppressed the surface reflection compared to the p-MS/Si substrate as well as the flat Si substrate though the NSs have truncated cone shapes with a low average height of ~ 200 nm, exhibiting the $R_{\text{avg}} \sim 9.1, 2.5,$ and 3.7% for Au film thicknesses of 5, 10, and 15 nm, respectively. These values are much lower than those of the p-MS/Si substrate as well as the flat Si substrate. This is caused by the linearly and continuously graded effective refractive index distribution from air to the Si via NSs, which is related to the so-called moth eye effect.¹⁷ Especially, at the Au film thickness of 10 nm, the NSs on the p-MS/Si substrate showed a superior antireflection property compared to the other samples at 5 and 15 nm. This is because the surface reflection is strongly dependent on the period and height of NSs.^{18–21} When the light with a normal incidence angle

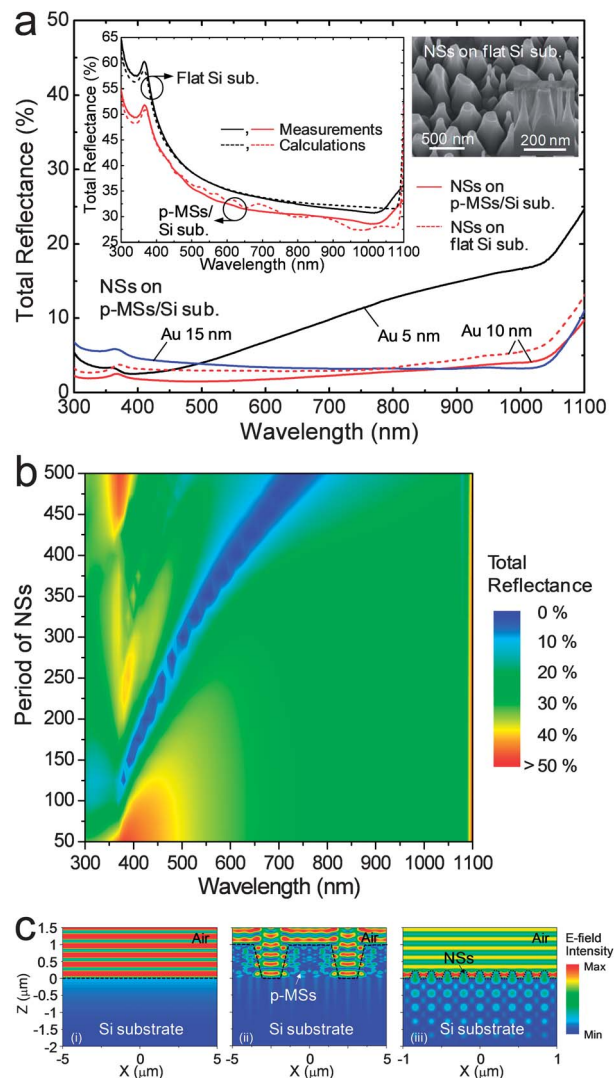


Fig. 3 (a) Measured total reflectance spectra of the fabricated NSs on p-MS/Si substrates for different Au film thicknesses of 5, 10, and 15 nm, (b) contour plot of variations of calculated total reflectance as functions of the period of NSs and wavelength for the NSs on the flat Si substrate, and (c) E-field intensity distributions ($\lambda = 550$ nm) of (i) the flat Si substrate, (ii) the p-MS/Si substrate, and (iii) the NSs on the flat Si substrate. The insets of (a) show the measured (solid lines) and calculated (dashed lines) total reflectance spectra (left) of the flat Si substrate and the p-MS/Si substrate and the 30° -tilted oblique- and side-view SEM images (right) of the fabricated NSs on the flat Si substrate for the Au film thickness of 10 nm.

of 0° enters the grating structure with a period of Λ , the angle of the reflected diffraction waves, $\theta_{r,m}$ in the m -th diffraction order is given by the grating equation:²²

$$\sin \theta_{r,m} = \frac{m\lambda}{\Lambda n}, \quad (1)$$

where n is the refractive index of incident medium and λ is the incident wavelength of light. If the period becomes much smaller than the wavelength of incident light, only the zeroth order diffracted light wave is allowed to propagate and all the higher orders are evanescent.^{20,23} Thus, the NSs with a smaller period than the incident light wavelength effectively reduce the surface reflection. On the other hand, although the period of NSs is very small, if their height is low, the reflectance is

increased at longer wavelengths.^{19,20} For the NSs on the p-MS/Si substrate, therefore, at 5 nm of Au thickness (average period of 50 nm), the reflectance is low at short wavelengths around 400 nm and then increased with wavelength owing to their low height. At 15 nm (average period of 360 nm), the reflectance is high at short wavelengths due to the higher order diffractive light while it becomes lower at long wavelengths around 900 nm owing to their longer period. At 10 nm (average period of 210 nm), however, the sample exhibits the lowest reflection characteristics over a wide wavelength region of 300–900 nm because of its desirable period and height. Also, for 10 nm, the reflectance spectrum of the NSs on the p-MS/Si substrate was lower than that of NSs on the flat Si substrate at wavelengths of 300–1100 nm. This may be attributed to the introduction of p-MSs into the NS/Si substrate. For the NSs on the p-MS/Si substrate with different Au film thicknesses, moreover, the lowest region in the reflectance was generally shifted towards the longer wavelengths with increasing the Au film thickness which determines the average period of NSs.¹⁸ This is attributed to the zeroth order diffracted wave at the corresponding wavelengths due to the smaller periods than the incident light wavelength, as mentioned above. For a theoretical optical analysis of the compound eye structure consisting of NSs on MSs at normal incidence, as can be found in our previous report,⁵ the NSs on the flat surface can be used due to the weak variation in the reflectance for the p-MSs (in the left inset of Fig. 3(a)). Thus, we showed the reflectance simulation results of the NSs on the flat Si substrate to theoretically analyze roughly the optical reflectance properties of the NSs on MSs as a function of the period of NSs at normal incidence. The 3D simulation model of the NSs on the flat Si substrate used in this calculation is shown in Fig. S1(b) of the ESI.† For the period of NSs, indeed, the calculated results in Fig. 3(b) roughly showed a similar trend to the experimentally measured data in Fig. 3(a). Additionally, the antireflection characteristics of the p-MSs and NSs can be observed in the calculated E-field intensity distributions at $\lambda = 550$ nm. In Fig. 3(c), for the flat Si substrate and the p-MS/Si substrate, the E-field intensity is high in the air region due to their strong surface reflection. For the NSs on the flat Si substrate, however, there exists a relatively weaker E-field intensity in the air region (stronger E-field intensity in the Si substrate) due to the low reflectivity caused by the graded effective refractive index profile between air and the Si *via* NSs. For solar cell applications, it is necessary to investigate the solar weighted reflectance (R_{SWR}), defined by the ratio of the usable photons reflected to the total useable photons, of samples. The R_{SWR} can be evaluated by normalizing the reflectance and the terrestrial AM1.5g spectra integrated over a wavelength range of 300–1030 nm.²⁴ The R_{SWR} is given by the following equation:

$$R_{\text{SWR}} = \frac{\int_{\lambda_1}^{\lambda_2} F(\lambda)R(\lambda)d\lambda}{\int_{\lambda_1}^{\lambda_2} F(\lambda)d\lambda}, \quad (2)$$

where $F(\lambda)$ is the photon flux density under the condition of AM1.5g and $R(\lambda)$ is the surface reflectance. For the NSs on p-MS/Si substrates at 10 nm of Au film thickness, the R_{SWR} value was

estimated to be $\sim 2\%$, indicating a lower value than that (*i.e.*, $R_{\text{SWR}} \sim 4.5\%$) of the NSs on the flat Si substrate at 10 nm as well as those of other structures (*i.e.*, $R_{\text{SWR}} \sim 7.4\%$ at 5 nm of the Au film and $\sim 3.6\%$ at 15 nm for the NSs on p-MS/Si substrates, respectively).

Fig. 4 shows the measured angle-dependent specular reflectance spectra of the (a) NSs on the flat Si substrate and (b) NSs on the p-MS/Si substrate for Au film thickness of 10 nm at different incident angles (θ_i) of 20–70° for un-polarized light. The R_{avg} and R_{SWR} values (left) of the corresponding structures as a function of θ_i and the side-view SEM image (right) of the NSs on the p-MS/Si substrate are shown in Fig. 4(b), respectively. For the NSs on the flat Si substrate, the specular reflectance spectra were also increased with increasing the θ_i . At θ_i values larger than 50°, particularly, there is an abrupt variation in the reflectance. For the NSs on the p-MS/Si substrate, however, the specular reflectance spectra were nearly not changed in the wavelength region of 300–1100 nm up to $\theta_i = 50^\circ$. Especially, the introduction of MSs into the NS/Si substrate leads to a significant decrease of the specular reflectance at short wavelengths of

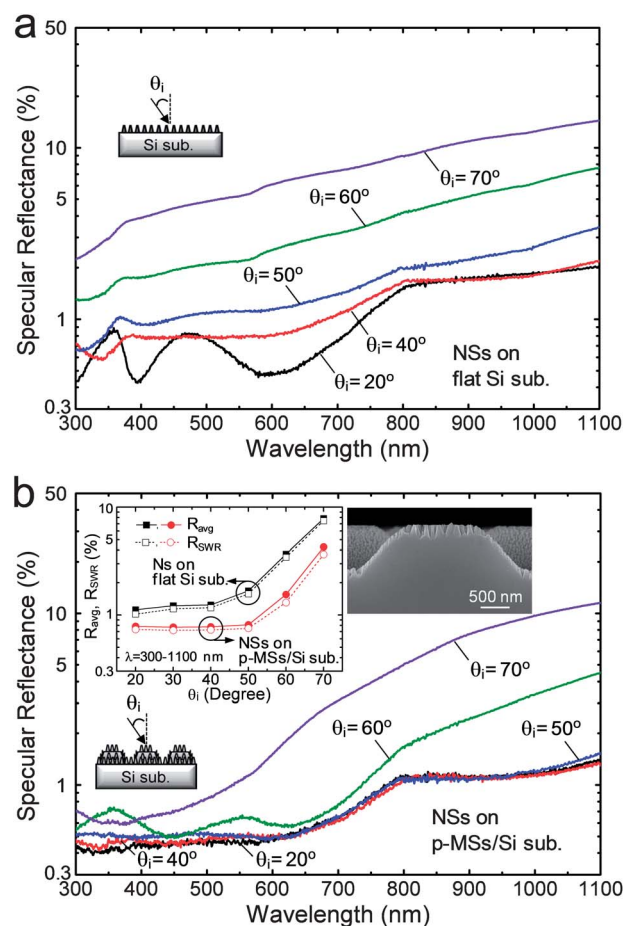


Fig. 4 Measured angle-dependent specular reflectance spectra of (a) the NSs on the flat Si substrate and (b) the NSs on the p-MS/Si substrate for Au film thickness of 10 nm at different incident angles (θ_i) of 20–70° for un-polarized light. The R_{avg} and R_{SWR} values (left) of the corresponding structures as a function of θ_i and the side-view SEM image (right) of the NSs on the p-MSs/Si substrate are shown in (b), respectively.

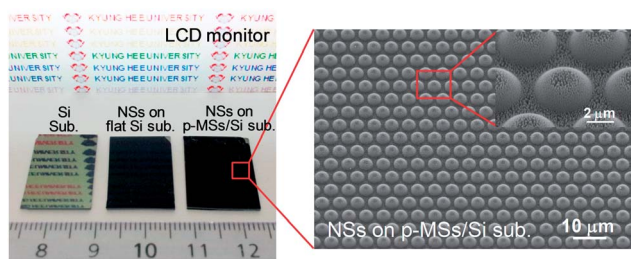


Fig. 5 (a) 50°-tilted oblique-view photograph of samples for the Si substrate and the NSs on the flat Si substrate and on the p-MS/Si substrate for Au film thickness of 10 nm. The 30°-tilted oblique-view zoom-out SEM images of the NSs on the p-MS/Si substrate are also shown.

300–700 nm over a wide θ_i range of 20–70°, maintaining low reflectance values below $\sim 3\%$ (i.e., $\sim 7.3\%$ for the NSs on the flat Si substrate). This is ascribed to the omnidirectionally aligned geometry of the truncated cone MSs, as shown in the SEM image of the inset of Fig. 4(b). Furthermore, in the wavelength range of 300–1100 nm, the R_{avg} and R_{SWR} values of the NSs on the p-MS/Si substrate were lower than those of the NSs on the flat Si substrate, exhibiting the $R_{\text{avg}} < 4.3\%$ and $R_{\text{SWR}} < 3.7\%$ at $\theta_i = 20\text{--}70^\circ$, respectively (i.e., $R_{\text{avg}} < 7.9\%$ and $R_{\text{SWR}} < 7.5\%$ for the NSs on the flat Si substrate), as can be seen in the left inset of Fig. 4(b). As a result, the NSs incorporated with the MSs can further reduce the Fresnel surface reflection losses over a wide wavelength region of 300–1100 nm for any incident angles including the normal incidence.²⁵

Fig. 5 shows the 50°-tilted oblique-view photograph of samples of the Si substrate and the NSs on the flat Si substrate and on the p-MS/Si substrate for Au film thickness of 10 nm. The 30°-tilted oblique-view zoom-out SEM images of the NSs on the p-MS/Si substrate are also shown. The characters in the LCD monitor were strongly reflected by the surface of the Si substrate. In contrast, the sample of the fabricated NSs on the flat Si substrate had almost a black surface but the characters were dimly reflected. For the NSs on the p-MS/Si substrate, however, the perfect dark black surface without any reflected characters was achieved. Absolutely, this fact confirms their low surface reflectivity at the high $\theta_i = 50^\circ$ at visible wavelengths, as shown in Fig. 4(b). From the SEM images of Fig. 5, it can be also observed that the fabricated NSs on the p-MS/Si substrate were very uniform and closely packed over a large area.

Conclusions

The compound eye structures consisting of the NSs on the top of p-MS/Si substrates were fabricated by dry etching using the photolithographic PR micropatterns and the thermally dewetted Au nanopatterns. The antireflection properties were investigated in the wavelength region of 300–1100 nm, together with the theoretical analysis using the RCWA method. The geometric profile and antireflection properties of the fabricated NSs on p-MS/Si substrates were strongly dependent on the Au film thickness. By introducing the p-MSs into NSs, the surface reflection was further reduced compared to the NSs on the flat Si substrate. For the Au film thickness of 10 nm, the NSs on the

p-MS/Si substrate decreased the R_{avg} and R_{SWR} values to $\sim 2.5\%$ and 2% over a wavelength range of 300–1030 nm, respectively, for the total reflectance at a near normal incident angle of $\sim 8^\circ$. At the high $\theta_i = 70^\circ$, in addition, the sample also exhibited the $R_{\text{avg}} < 4.3\%$ and $R_{\text{SWR}} < 3.7\%$ at wavelengths of 300–1100 nm in angle-dependent specular reflectance measurements. The theoretically calculated reflectance results by the RCWA simulation showed similar trends with the experimentally measured data. The compound eye architectures made of the NSs on top of p-MS/Si substrates can provide the omnidirectional broadband antireflection characteristics for Si-based optical and optoelectronic device applications.

Acknowledgements

This research was supported by the Basic Science Research Program through the National Research Foundation of Korea (NRF) funded by the Ministry of Science, ICT and Future Planning (no. 2013-010037).

Notes and references

- 1 K. H. Jeong, J. Kim and L. P. Lee, *Science*, 2006, **312**, 557.
- 2 X. Gao, X. Yan, X. Yao, L. Xu, K. Zhang, J. Zhang, B. Yang and L. Jiang, *Adv. Mater.*, 2007, **19**, 2213.
- 3 P. Vukusic and J. R. Sambles, *Nature*, 2003, **424**, 852.
- 4 J. Huang, X. Wang and Z. L. Wang, *Nanotechnology*, 2008, **19**, 025602.
- 5 Y. M. Song, G. C. Park, S. J. Jang, J. H. Ha, J. S. Yu and Y. T. Lee, *Opt. Express*, 2011, **19**, A157.
- 6 J. W. Leem and J. S. Yu, *Thin Solid Films*, 2011, **519**, 3792.
- 7 H. Park, S. Choi, S. Lee and K. H. Koh, *J. Vac. Sci. Technol., B: Microelectron. Nanometer Struct.–Process., Meas., Phenom.*, 2004, **22**, 1290.
- 8 K. C. Sahoo, M. K. Lin, E. Y. Chang, Y. Y. Lu, C. C. Chen, J. H. Huang and C. W. Chang, *Nanoscale Res. Lett.*, 2009, **4**, 680.
- 9 S. Wang, X. Z. Yu and H. T. Fan, *Appl. Phys. Lett.*, 2007, **91**, 061105.
- 10 J. Zhao, *Sol. Energy Mater. Sol. Cells*, 2004, **82**, 53.
- 11 Z. Huang, J. E. Carey, M. Liu, X. Guo, E. Mazur and J. C. Campbell, *Appl. Phys. Lett.*, 2006, **89**, 033506.
- 12 J. M. Lee and B. I. Kim, *Mater. Sci. Eng., A*, 2007, **449–451**, 769.
- 13 P. L. Redmond, A. J. Hallock and L. E. Brus, *Nano Lett.*, 2005, **5**, 131.
- 14 M. G. Moharam and T. K. Gaylord, *J. Opt. Soc. Am.*, 1981, **71**, 811.
- 15 S. Y. Chuang, H. L. Chen, J. Shieh, C. H. Lin, C. C. Cheng, H. W. Liu and C. C. Yu, *Nanoscale*, 2010, **2**, 799.
- 16 M. L. Kuo, D. J. Poxson, Y. S. Kim, F. W. Mont, J. K. Kim, E. F. Schubert and S. Y. Lin, *Opt. Lett.*, 2008, **33**, 2527.
- 17 P. B. Clapham and M. C. Hutley, *Nature*, 1973, **244**, 281.
- 18 S. A. Boden and D. M. Bagnall, *Appl. Phys. Lett.*, 2008, **93**, 133108.
- 19 Y. M. Song and Y. T. Lee, *Opt. Quantum Electron.*, 2009, **41**, 771.

- 20 Y. M. Song, H. J. Choi, J. S. Yu and Y. T. Lee, *Opt. Express*, 2010, **18**, 13063.
- 21 J. W. Leem, Y. M. Song, Y. T. Lee and J. S. Yu, *Appl. Phys. B: Lasers Opt.*, 2010, **100**, 891.
- 22 E. Hecht, *Optics*, Addison Wesley, 4th edn, 2002, ch. 10.
- 23 J. W. Leem, Y. Yeh and J. S. Yu, *Opt. Express*, 2012, **20**, 4056.
- 24 D. Redfield, *Sol. Cells*, 1981, **3**, 27.
- 25 Y. Wang, N. Lu, H. Xu, G. Shi, M. Xu, X. Lin, H. Li, W. Wang, D. Qi, Y. Lu and L. Chi, *Nano Res.*, 2010, **3**, 520.